Nanotechnology

PURPOSE-LED PUBLISHING™

Integration of InP membranes with embedded InGaAs quantum wells on silicon-on-insulator by tunnel epitaxy

To cite this article before publication: Zhao Yan *et al* 2026 *Nanotechnology* in press https://doi.org/10.1088/1361-6528/ae4985

Integration of InP membranes with embedded InGaAs quantum wells on silicon-on-insulator by tunnel epitaxy

Zhao Yan [1]*, Tim Grieb [2], Weiwei Zhang [3], Martin Ebert [3], Florian F. Krause [2], Graham T. Reed [3], David J. Thomson [3], Andreas Rosenauer [2] and Qiang Li [1]*

[1] School of Physics and Astronomy, Cardiff University, Cardiff CF24 3AA, UK

[2] Institute of Solid State Physics, University of Bremen, 28359 Bremen, Germany

[3] Optoelectronics Research Centre, University of Southampton, Southampton SO17 1BJ, UK

* Authors to whom any correspondence should be addressed.

E-mail: YanZ19@cardiff.ac.uk and LiQ44@cardiff.ac.uk

Abstract

Integration of III–V membranes on silicon-on-insulator (SOI) substrates offers a promising route to provide on-chip gain for dense silicon (Si) photonics. Here, we present a materials study of InP membranes with embedded InGaAs multi-quantum wells (MQWs) directly grown above the Si waveguide layer via a tunnel epitaxy process. Cross-sectional scanning transmission electron microscopy (STEM), combining differential phase contrast (DPC) imaging, energy-dispersive X-ray spectroscopy (EDX), and atomic-column-based strain analysis, confirms high-quality laterally grown InP membranes with defects confined to the V-groove region and elucidates facet-dependent MQW formation on (111)A, (110), and (111)B facets. Both EDX and strain analysis consistently reveal high-In, highly compressively strained (110) QWs (>80% In), and no misfit dislocations are observed at InP/InGaAs interfaces. In addition, under identical precursor ratios, ultra-thin QWs incorporate a higher indium composition than a thick bulk InGaAs region. These results provide practical guidance for designing efficient active regions in future electrically injected, Si-waveguide-coupled InP membrane lasers on SOI.

Introduction

Silicon (Si) photonics has emerged as a versatile platform enabling a wide range of applications including data communications, optical sensing, and quantum photonics.[1-5] Monolithic integration of III-V gain materials on Si photonic chips for light emitting and amplification is considered a promising route toward high-density Si photonic systems beyond the current heterogeneous integration paradigm.[6-10] Among various epitaxial integration approaches, selective area growth of quantum dot lasers and aspect ratio trapping (ART) growth of nano-ridge lasers on patterned Si wafers have shown great promise.[8,11-19] However, neither of the two integration schemes make use of the mainstream silicon-on-insulator (SOI) platform on which heterogeneous integration has flourished. For the quantum dot laser approach, tacking the challenges associated with the epitaxial growth in cavities and the coupling with the Si waveguides remain critical tasks. For the III–V nano-ridges lasers, adapting device fabrication

to accommodate the unique shape and dimension of the ridge structure, particularly around the metal contacts and efficient electrical injection, is not trivial. Recent progress in lateral growth techniques have introduced a new monolithic integration platform to bring III-V functions to the Si photonics SOI platform.[20-29] The thick buffer layers commonly required to overcome the lattice mismatch in conventional heteroepitaxy is no longer needed. III-V-on-insulators with lateral pin junctions and lateral heterostructure can be realized, opening new avenues for the design of integrated photonic devices. Recently, we developed a tunnel epitaxy process to grow large-dimension InP membranes on top of an insulator layer above the Si device layer of the SOI substrate.[30]

In this work, we investigate InGaAs multiple quantum wells (MQWs) embedded in laterally grown InP membranes on SOI enabled by the tunnel epitaxy approach. The crystalline quality, composition, and strain of the MQWs are examined by cross-sectional scanning transmission electron microscopy (STEM), combining differential phase contrast (DPC) imaging with energy-dispersive X-ray spectroscopy (EDX) mapping and atomic-resolution strain analysis. We demonstrate high-quality InP membranes on SOI, and show that both EDX and strain analysis consistently reveal high-In, highly compressively strained (110) QWs (>80% In) embedded within the membranes. Despite the large mismatch, no misfit dislocations are observed in the MQWs even when the QW thickness exceeds the nominal (110) critical thickness, which we attribute to the finite membrane thickness and the associated elastic compliance. We also observe that, under identical precursor ratios, ultra-thin QWs can incorporate more indium than a thick bulk InGaAs region. Overall, these findings support lateral membrane growth as a practical platform for integrating high-strain (110) MQWs on SOI and the design of membrane-based active regions for Si-photonic lasers.

Results and discussion

Figure 1 illustrates the integration of InP membranes on Si waveguides using the tunnel epitaxy approach. The initial epitaxial growth within the Si V-grooves provides high-quality InP seed layers, which facilitate the subsequent lateral expansion of InP membranes atop the Si waveguides. As shown in the schematic of Figure 1a, the InP membranes can be positioned either on the Si layer or on the SiO_2 cladding and the Si waveguides. These configurations are illustrated by the optical microscope images in Figures 1b and 1c, where the membranes are located on top of the Si layer and the SiO_2 cladding, respectively. Top-view and tilted view scanning electron microscopy (SEM) images in Figures 1d and 1e further demonstrate the integration structure, showing the InP membranes grown from the V-groove (lower-left corner) and sandwiched between two silicon nitride (SiN) layers on top of the Si waveguide layer. Within the same SOI geometry, we did not observe a noticeable difference in the InP membrane growth when the membrane is formed above the Si device layer versus above the buried SiO_2 cladding. In this work we use the InP/SiN/Si configuration as a representative platform for the detailed study presented below.

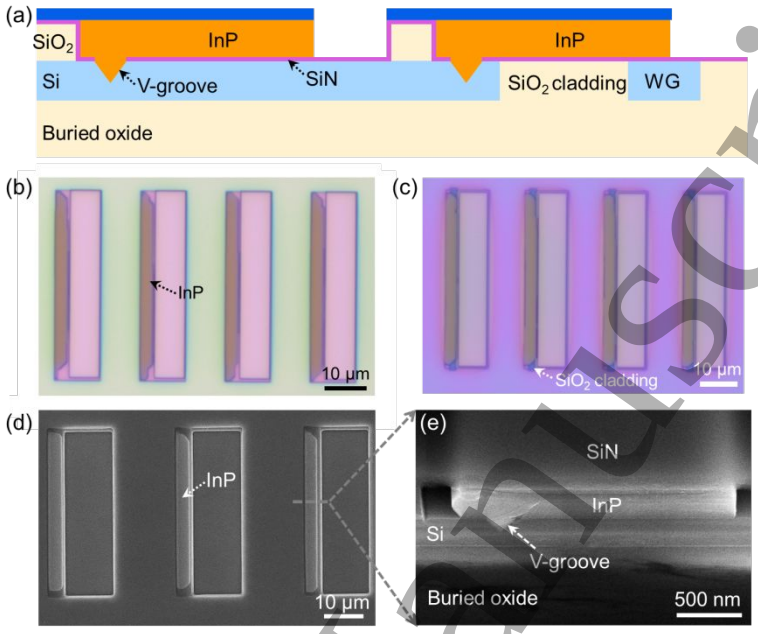

Fig. 1. (a) Schematic illustration of the integration of InP membranes on Si waveguide layer as well as on SiO_2 and Si waveguides via tunnel epitaxy. (b, c) Optical microscope images showing InP membranes grown on Si waveguide layer and on the buried SiO_2 cladding, respectively. (d) Top-view SEM image of epitaxial InP membranes, where the InP beneath the top SiN layer is visible. (e) Tilted-view (45° tilted) SEM image showing the InP membrane grown laterally from the Si V-groove at the lower-left corner.

The epitaxy of InP membranes and InGaAs MQWs was performed using an Aixtron close coupled showerhead metal organic chemical vapor deposition (MOCVD) system. TMIn and TEGa were used as the group III precursors; TBAs and TBP were used as the group V precursors. Figure 2a shows a STEM image recorded with a high angle annular dark field (HAADF) detector, illustrating the transition from vertical V-groove growth to lateral membrane expansion. The corresponding DPC image is presented in Figure 2b. The DPC imaging was obtained using a Thermo Fisher Panther detector, which consists of different segments, recording the diffracted electron intensity in four angular regions at the same time. The difference in intensity between opposite directions is highly sensitive to, e.g., crystal orientation; consequently, changes in crystallinity (such as defects) are easily visible. In the colored DPC images, the average direction of the diffracted intensity is shown qualitatively. The color visualizes the direction, and brightness reflects the magnitude. The varying color contrast inside and near the V-groove in the DPC image is due to the presence of crystal defects, whereas the laterally grown InP membrane region maintains uniform contrast, suggesting homogeneous single crystalline materials.

Zoomed-in STEM images of the V-groove region are shown in Figures 2c and 2e, revealing stacking faults (SFs) propagating along the (111) crystal planes. These structural imperfections are also reflected in the corresponding DPC images (Figures 2d and 2f). Additionally, a thin

SiN layer is visible atop the Si waveguide layer (Figure 2c), serving as a growth mask during the epitaxial growth.

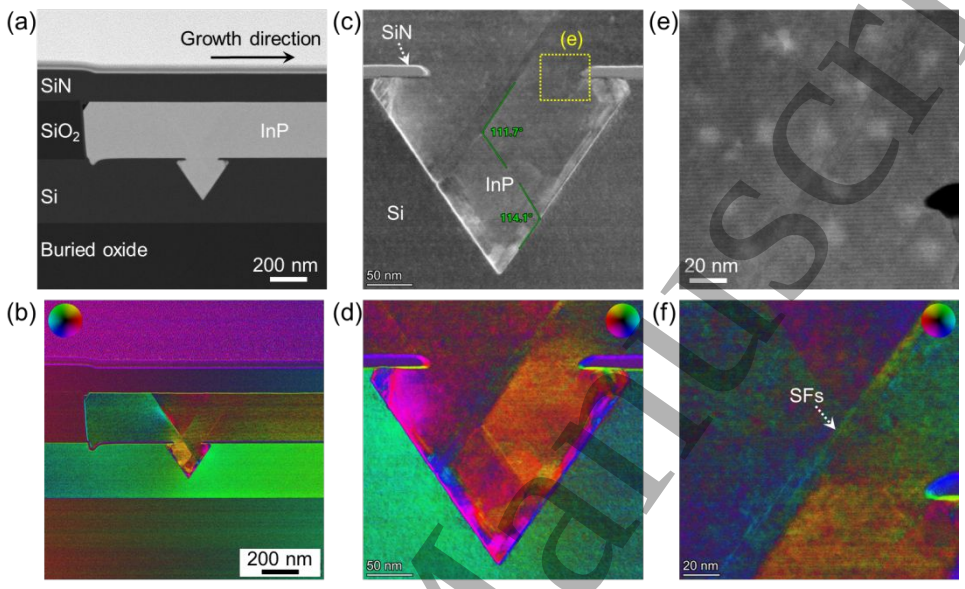

Fig. 2. (a) STEM image showing the growth transition of InP from the Si V-groove to the lateral growth, and corresponding DPC image (b) highlighting the single-crystalline phase of the lateral InP membrane away from the V-groove. (c, e) Enlarged STEM images at the V-groove region revealing defects formation at initial Si V-groove, and corresponding DPC images (d, f) reflecting the presence of crystalline defects originating from the V-groove.

Following the successful formation of the InP membranes, InGaAs MQWs were incorporated during the lateral epitaxial growth step. The quantum wells were grown at 620 °C, with an indium-to-group-III gas-phase ratio of 53% and a V/III ratio of 30. The MQW morphology was then examined by SEM. To clearly reveal the MQW structures, a phosphoric acid-based etchant (H_3PO_4:H_2O_2:H_2O = 3:1:50; etch time ~30 s) was used to selectively remove InGaAs relative to the surrounding InP. Figure 3 summarizes the facet orientations observed in the InP/InGaAs membranes. Three distinct facets were identified: a vertical (110) facet and two inclined, (111)A and (111)B, facets. As indicated by Figure 3a, MQW formation can proceed via different faceting outcomes: a vertical (110) facet supporting vertical (110) MQWs (upper image), or a morphology dominated by the inclined (111) facets (lower image). The detailed analysis below focuses on the former, while the latter motivates further optimization of InP facet evolution to stabilize the (110) facet for uniform MQW formation. The SEM image in Figure 3a shows the facet orientations, while the crystallographic schematic in Figure 3b presents their corresponding formation.

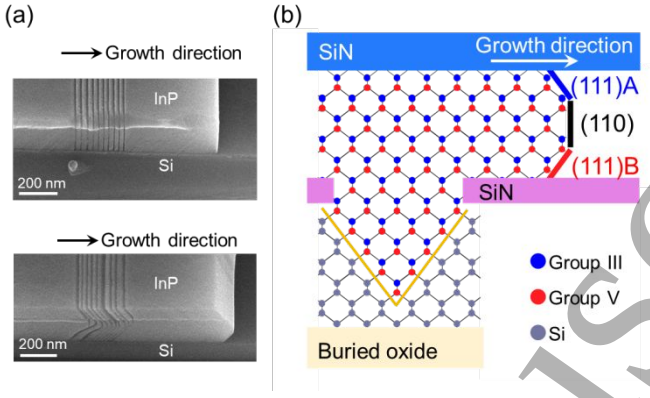

Fig. 3. (a) Tilted SEM images: top, InGaAs MQW with predominantly vertical (110) facets; bottom, InGaAs MQW with inclined (111)A and (111)B facets. (b) Crystallographic diagram illustrating the (110), (111)A and (111)B facets.

We performed cross-sectional STEM on the InP/InGaAs membrane to elucidate the structural characteristics of the InGaAs MQWs. Figure 4a presents a STEM overview of a sample exhibiting predominantly vertical (110) faceting (corresponding to the upper SEM image in Figure 3a). The InP membrane is originated from the Si V-groove at the lower left, and positioned above the Si waveguide layer. Within the horizontal InP membrane, ten periods of InGaAs MQWs are clearly resolved, as shown in the magnified STEM image in Figure 4b. The MQWs are mainly formed on the vertical (110) facet, while two small, inclined facets, (111)A at the upper side and (111)B at the lower side, are also present, as indicated by the crystallographic diagram in Figure 3b. The emergence of these (111)A and (111)B facets is attributed to interfacial-energy minimization at the III–V/dielectric boundary, a feature also observed in selective-area III–V growth by ART.[31,32]

As indicated in Figure 4b, the InGaAs QW thickness on the vertical (110) facet is ~7.8 nm. The InGaAs thickness on the upper (111)A facet is comparable to, or slightly larger than, that on (110) under present growth conditions, whereas the QW on the bottom (111)B facet is substantially thinner. In particular, once the (111)B facet becomes well defined, InGaAs growth on the (111)B is negligible (<0.5 nm). By optimizing growth conditions, previous studies have demonstrated that it is possible to engineer buried (110) InGaAs MQWs within lateral InP membranes while suppressing InGaAs deposition on (111)A facets.[33,34] Figure 4c shows a close-up STEM view of the vertical (110) InP/InGaAs MQWs, highlighting sharp and well-defined QW interfaces. Figure 4d focuses on the bottom (111)B facet region, where the InP/InGaAs membrane is positioned above the Si waveguide layer and separated by a thin SiN spacer (~12 nm).

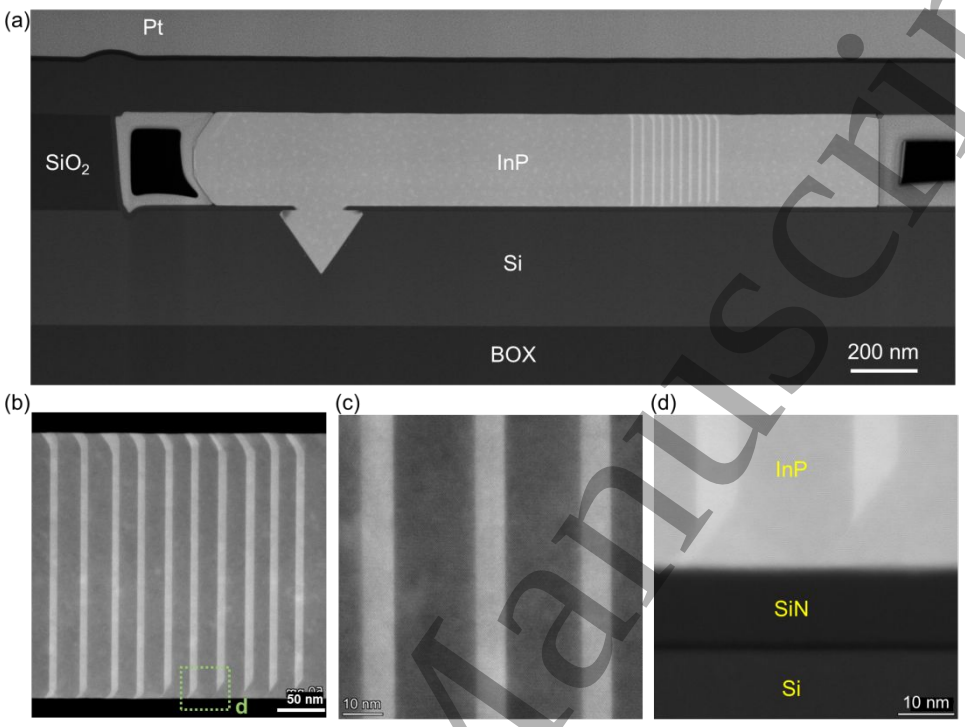

Fig. 4. (a) STEM overview of an InP membrane containing a 10-period InGaAs/InP MQW. (b) Enlarged STEM image of the MQWs, highlighting facet-dependent InGaAs well thickness on the (110), (111)A, and (111)B facets. (c) Close-up STEM image of the vertical (110) MQWs, showing sharp InP/InGaAs interfaces. (d) Close-up STEM image at the bottom (111)B region, where the InP/InGaAs membrane is positioned above the Si waveguide layer and separated by a thin SiN spacer.

We further examined the InGaAs MQWs by STEM in combination with EDX. Figure 5a identifies the region of interest containing the 10-period MQW stack and the InGaAs MQWs with the (111)A, (110), and (111)B facets. An EDX line scan was acquired along the direction indicated by the green arrow in Figure 5a, and Figure 5b presents the resulting compositional profile across the ten MQW periods. To compare the compositions on different facets, EDX area measurements were also taken from the (111)A and (110) facets. The probed positions are marked in Figure 5c, where areas #1 and #1A correspond to the (110) and (111)A facets of the same quantum well. In total, the ten probed areas span five InGaAs QWs. The corresponding indium compositions are plotted in Figure 5d. While a slight well-to-well variation is observed, the extracted indium compositions show minimal difference between the (111)A and (110) facets within the same InGaAs well.

Figure 5e shows the 10-period MQW stack formed on the vertical (110) facet with a uniform QW thickness, together with the corresponding EDX elemental maps. Ten regions within the InGaAs wells (labelled #1–10 in Figure 5e) were selected for EDX area measurements, and the resulting compositions are summarized in Figure 5f. The indium compositions obtained from these ten (110)-facet wells are comparable with the value inferred from the line-scan profile in Figure 5b. From the EDX, the indium composition in the InGaAs wells is approximately 85%.

It should be noted that the EDX-derived indium composition may be inflated due to the surrounding InP barrier and the narrow width of the quantum wells.

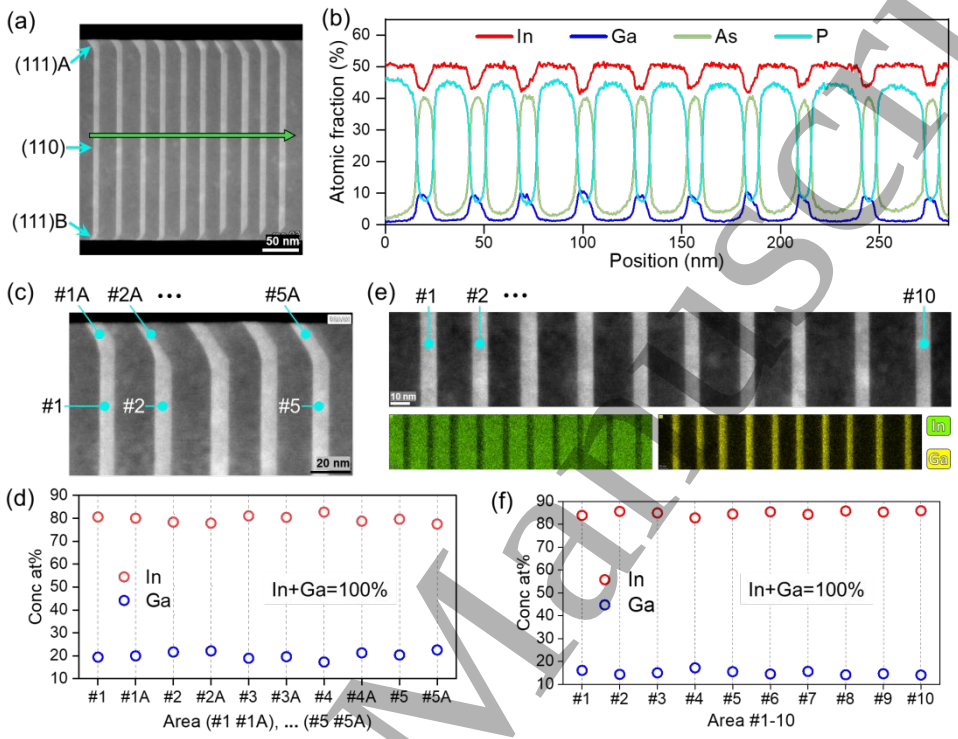

Fig. 5. EDX line-scan and area analyses of the InGaAs/InP MQWs. (a) STEM image of the MQW region for EDX measurements. (b) EDX line profile acquired along the arrow-marked path in (a), resolving the 10-period MQW stack. (c) Locations selected for EDX area analysis on the (110) and (111)A facets (e.g., #1 and #1A) within each InGaAs wells, and (d) corresponding indium compositions. (e) STEM image and corresponding EDX elemental mapping of the 10-period MQWs on the vertical (110) facet. (f) Summary of EDX area analysis (#1–#10) performed within the (110) InGaAs wells marked in (e).

We then performed a strain analysis on the (110)-orientated InGaAs QWs to extract the indium compositions. This analysis is enabled by atomic-resolution STEM, which provides direct access to the atomic-column positions for quantitative fitting. Figure 6a shows a close-up STEM image of a representative vertical (110) QW. From the fitted atomic positions, we extracted the local inter-column spacings along two orthogonal directions in the image. Figure 6b presents the local spacing between neighboring atomic columns along the horizontal direction, normalized to the average spacing in the image. A larger spacing is observed within the InGaAs well region compared with the adjacent InP barriers. In contrast, the spacing along the vertical direction (Figure 6c) remains comparatively uniform across both the InP and InGaAs regions. Figure 6d summarizes the statistical distribution of the horizontal spacing extracted from Figure 6b (horizontal spacing). Using InP as a reference (approximating the adjacent InP barriers as locally unstrained), the lattice mismatch along the lateral-growth direction within the InGaAs QW is determined to be $\varepsilon_{\perp}$= 3.34%.

From this observation, the free-standing (relaxed) lattice constant a_0 of the InGaAs QW can thus be calculated and the indium composition can also be extracted. Cross-sectional STEM indicates that the lattice-column spacing along the growth direction [110] is 3.34% larger than InP, while the in-plane spacing remains matched to InP; we therefore set $a_{//} = a_{\mathrm{InP}} = 5.8687\text{Å}$ and obtain $a_\perp$ from the measured [110] spacing by noting that, for a cubic lattice, the (110) interplanar spacing is $d_{110} = a/\sqrt{2}$, i.e. $a_\perp = \sqrt{2}\, d_{110}$ (hence a 3.34% increase in d_{110} corresponds to the same 3.34% increase in $a_\perp$).

To extract the relaxed lattice constant a_0 of the InGaAs QW, we use biaxial elasticity. Under pseudomorphic biaxial strain, the in-plane strain is constrained by the InP barrier, while the free-surface (traction-free) condition along the growth normal requires $\sigma_{nn} = 0$. This links the out-of-plane and in-plane mismatches via $\varepsilon_\perp = -\nu\, \varepsilon_\parallel$, where ν is the orientation-dependent biaxial Poisson ratio (for the common (001) case, $\nu_{001} = 2C_{12}/C_{11}$). For the present (110) orientation, ν_{110} can be written as[35]:

$$\nu_{110} = \frac{C_{11}+3C_{12}-2C_{44}}{C_{11}+C_{12}+2C_{44}} \quad (1)$$

where C_{11},C_{12},C_{44} are the stiffness constants. The relaxed lattice constant is then obtained by substituting ν_{110} from Eq. (1) into

$$a_0 = \frac{a_\perp+\nu_{110}a_{//}}{1+\nu_{110}} \quad (2)$$

with $a_{//} = a_{\mathrm{InP}}$ and $a_\perp$ extracted from the measured (110) spacing. Using composition-dependent stiffness constants obtained by linear interpolation, Eqs. (1)–(2) were solved self-consistently with Vegard's law, giving $a_0 \approx 5.988$Å and an indium composition of 82.6% for the (110)-orientated InGaAs QW.

Therefore, both the EDX and the strain analysis indicate that the indium composition in the InGaAs QW is significantly higher than the indium-to-group-III gas-phase ratio of 53%, leading to compressively strained InGaAs MQWs as illustrated schematically in Figure 6e. This highlights a key advantage of the lateral-growth approach: it enables highly compressively strained, (110)-oriented InGaAs QWs with high indium content to be embedded within the InP membrane. Although the QW thickness (7.8 nm) is larger than the critical thickness expected for such a highly strained InP/InGaAs system,[33] cross-sectional STEM reveals no misfit dislocations at the (110) InP/InGaAs interfaces. We attribute this defect-free accommodation to the finite InP membrane thickness (~340 nm), which allows partial elastic compliance (and relief via nearby free surfaces), thereby reducing the driving force for misfit dislocation formation and increasing effective critical thickness in the thin-membrane heteroepitaxy.

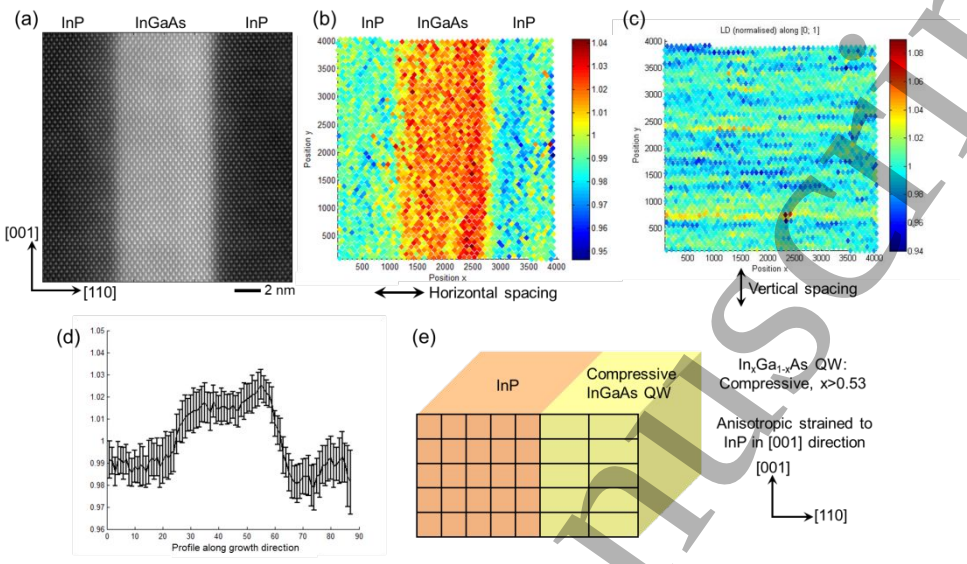

Fig. 6. Atomic-resolution STEM–based lattice-strain mapping of the (110)-orientated InGaAs QW embedded in InP membrane. (a) Atomic-resolution STEM image of the (110) InGaAs QW region used for strain analysis. (b) Map of the horizontal inter-atomic-column spacing (normalized to the mean value in the field of view), highlighting an expansion within the InGaAs well relative to the adjacent InP barriers. (c) Map of the spacing in the orthogonal direction (vertical), showing a comparatively uniform lattice spacing across both InP and InGaAs region. (d) Statistical summary of the extracted horizontal spacing from (b). A lattce mismatch $\varepsilon_{\perp}$= 3.34% is extracted. (e) Schematic illustrating the resulting anisotropic strain state of the vertical (110) QWs, characterized by a pronounced distortion along the lateral-growth direction and minimal change along the orthogonal (in-plane) direction.

Finally, we compare the thin (110) InGaAs QWs and a thick bulk InGaAs layer intentionally grown at the end of the InP membrane (Figure 7a, growth direction from right to left). The bulk layer was grown under exactly the same conditions as the QWs (indium-to-group-III gas-phase ratio of 53%) and has a lateral width of ~700 nm. Figure 7a shows an EDX map containing both the bulk InGaAs region and the 5-period InGaAs MQWs, and Figure 7b plots an EDX line profile taken along the arrow in Figure 7a. From the line profile, the bulk InGaAs exhibits an indium composition of ~50% (i.e. $In_{0.5}Ga_{0.5}As$), whereas the QWs show a much higher indium level (>80%), consistent with the strain-derived composition (In composition of 82.6%). Notably, the transition in the EDX line scan at the bulk InGaAs/InP interface spans ~15 nm in the x-axis (from bulk InGaAs to InP, indium increasing from ~50% to 100%), which likely reflects the finite spatial resolution/beam-spreading and associated cross-talk in STEM-EDX quantification. Therefore the composition extraction in an ultra-thin QW should be interpreted with care.[36]

Overall, these results indicate that the bulk InGaAs composition is close to the group-III gas-phase ratio under steady-state growth, whereas the ultra-thin QWs can deviate strongly and incorporate substantially more indium. A plausible explanation is that thick layers are dominated by thermodynamic-limited behavior, whereas in thin QWs the solid composition is more sensitive to surface-kinetic and interfacial-transient effects, which could bias indium incorporation upward even under identical input ratios.[37]

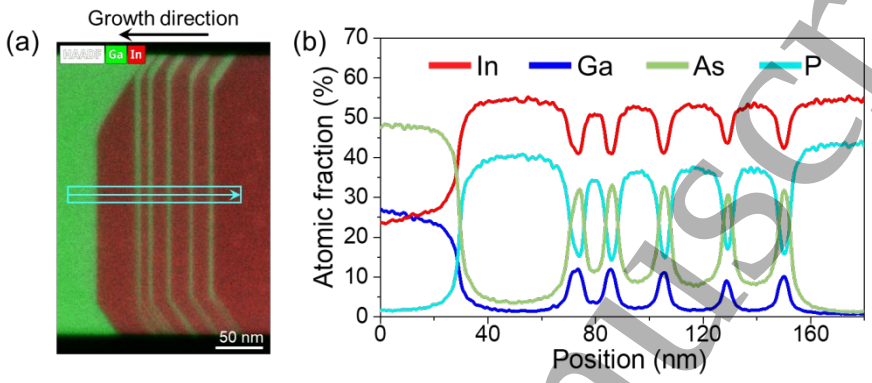

Fig. 7. (a) EDX maps showing both the bulk InGaAs and the InGaAs QW area. (b) EDX line profile acquired along the arrow-marked path in (a).

Conclusion

In conclusion, we have presented a comprehensive study of laterally grown InP membranes with embedded InGaAs MQWs integrated on SOI using the tunnel epitaxy approach. STEM combined with DPC imaging confirms the high crystalline quality of the InP membranes, with defects confined to initial V-groove region. Cross-sectional STEM further reveals clear MQW formation on (111)A, (110), and (111)B facets, showing a negligible deposition on (111)B facet. Both EDX and lattice-strain analysis indicate a high-In, highly compressively strained (110) QW (indium composition >80%). Despite the QW thickness (7.8 nm) exceeding the nominal (110) critical thickness, cross-sectional STEM shows no misfit dislocations at the InP/InGaAs interfaces, suggesting that the finite membrane thickness (~340 nm) and associated elastic compliance enable coherent accommodation of large mismatch. In addition, under identical precursor ratios, the ultra-thin (110) QWs incorporate a higher indium composition than a thick bulk InGaAs region. Future work will focus on optimizing the InP facet evolution to favour vertical (110) facet and thereby facilitate uniform (110)-oriented MQW formation. Overall, our study focus on the structure, composition, and strain analysis of high-In (110) MQWs embedded in laterally grown InP membranes on SOI substrates, providing practical guidance for implementing high-strain active regions in future electrically injected, Si-waveguide-coupled membrane lasers.

Acknowledgement

This work was supported by Engineering and Physical Sciences Research Council [EP/Z536167/1] and the Royal Society [ICA\R1\241147]. A.R. thanks the Deutsche Forschungsgemeinschaft (DFG, German Research Foundation) for funding of the Spectra300, project number 384546896.

Data Availability Statements

Data supporting the findings of this study are available at: https://doi.org/10.17035/cardiff.30017533

Conflict of interest

The authors declare no conflict of interest.

References

1. N. Margalit, C. Xiang, S. Bowers, A. Bjorlin, ... and J. Bowers, "Perspective on the future of silicon photonics and electronics", Appl. Phys. Lett. 118, 220501 (2021).
2. C. Xiang, W. Jin, D. Huang, M. A. Tran, ... and J. E. Bowers, "High-Performance Silicon Photonics Using Heterogeneous Integration", in IEEE Journal of Selected Topics in Quantum Electronics, vol. 28, no. 3 (2022).
3. S. Matsuo, and T. Kakitsuka, "Low-operating-energy directly modulated lasers for shortdistance optical interconnects", Adv. Opt. Photon. 10, 567-643 (2018).
4. D. Thomson, A. Zilkie, J. Bowers, T. Komljenovic, ... and M Nedeljkovic, "Roadmap on silicon photonics", J. Opt. 18 (2016) 073003 (20pp).
5. C. Zhang, M. Tran, Z. Zhang, A. Dorche, ... and T. Komljenovic, "Integrated photonics beyond communications", Appl. Phys. Lett. 123, 230501 (2023).
6. Z. Zhou, X. Ou, Y. Fang, E. Alkhazraji, ... and J. Bowers, Prospects and applications of on-chip lasers", eLight 3, 1 (2023)
7. Y. Wan, W. He, J. Jaussi, L. Liao, ... and H. Rong, "Integrating silicon photonics with complementary metal–oxide–semiconductor technologies", Nature Review Electr Eng (2025).
8. Y. Koninck, C. Caer, D. Yudistira, Marina Baryshnikova1, ... and J. V. Campenhout, "GaAs nano-ridge laser diodes fully fabricated in a 300-mm CMOS pilot line", Nature 637, 63–69 (2025).
9. Y. Han, H. Park, J. Bowers, and K. M. Lau, "Recent advances in light sources on silicon", Adv. Opt. Photon. 14, 404-454 (2022).
10. A. Y. Liu, and J. Bowers, "Photonic Integration with Epitaxial III–V on Silicon", IEEE J. of Selected Topics in Quantum Electronics, 24, no.6, pp. 1-12, 2018.
11. Z. Yan and Q. Li, "Recent progress in epitaxial growth of dislocation tolerant and dislocation free III–V lasers on silicon," J. Phys. D: Appl. Phys. 57(21), 213001 (2024).
12. C. Shang, K. Feng, E. T. Hughes, A. Clark, ... and J. E. Bowers, "Electrically pumped quantum-dot lasers grown on 300 mm patterned Si photonic wafers", Light: Science & Applications (2022) 11:299
13. W. Wei, A. He, B. Yang, Z. Wang ... and T. Wang, "Monolithic integration of embedded III-V lasers on SOI", Light: Science & Applications (2023) 12:84
14. R. Koscica et al., "Quantum Dot DBR Lasers Monolithically Integrated on Silicon Photonics by In-Pocket Heteroepitaxy," in Journal of Lightwave Technology, vol. 43, no. 12, pp. 5773-5781, 15 June15, 2025
15. Z. Yan, S. Liu, B. Ratiu, K. Wong, ... and Q. Li, "MOCVD-grown InAs/InP quantum dot lasers with low threshold current", Opt. Express 33, 31195-31203 (2025).
16. Y. Shi, Z. Wang, J. Campenhout, M. Pantouvaki, ... and D. Thourhout, "Optical pumped InGaAs/GaAs nano-ridge laser epitaxially grown on a standard 300-mm Si wafer" Optica 4, 1468-1473 (2017).

17. A. Yimam, D. Colucci, C. Caer, D. Yudistira, ... and G. Morthier, "Advanced characterization and parameter extraction of electrically injected InGaAs/GaAs nano-ridge lasers monolithically integrated on silicon", Opt. Express 33, 27929-27941 (2025).

18. W. Guo, Y. Mols, J. Belz, A. Beyer, ... and B. Kunert, "Anisotropic relaxation behavior of InGaAs/GaAs selectively grown in narrow trenches on (001) Si substrates", J. Appl. Phys. 122, 025303 (2017)

19. Y. Han, Z. Yan, W. K. Ng, Y. Xue, ... and K. M. Lau, "Bufferless 1.5 μm III-V lasers grown on Si-photonics 220 nm silicon-on-insulator platforms", Optica 7, 148-153 (2020).

20. Z. Yan, Y. Han, L. Lin, Y. Xue, ... and K. M. Lau, "A monolithic InP/SOI platform for integrated photonics", Light: Science & Applications (2021) 10:200.

21. Y. Xue, Y. Han, Y. Tong, Z. Yan, ... and K. M. Lau, "High-performance III-V photodetectors on a monolithic InP/SOI platform", Optica 8, 1204-1209 (2021).

22. P. Wen, P. Tiwari, S. Mauthe, H. Schmid, ... and K. E. Moselund, "Waveguide coupled III-V photodiodes monolithically integrated on Si", Nat Commun 13, 909 (2022).

23. L. Czornomaz, E. Uccelli, M. Sousa, V. Deshpande, ... and J. Fompeyrine, "Confined Epitaxial Lateral Overgrowth (CELO): A Novel Concept for Scalable Integration of CMOS-compatible InGaAs-on-insulator MOSFETs on Large-Area Si Substrates", 2015 Symposium on VLSI Technology (VLSI Technology), Kyoto, Japan, 2015, pp. T172-T173, doi: 10.1109/VLSIT.2015.7223666.

24. M. Borg, L. Gignac, J. Bruley, A. Malmgren, ... and H. Schmid, "Facet-selective group-III incorporation in InGaAs template assisted selective epitaxy", Nanotechnology 30 (2019) 084004 (8pp)

25. Z. Yan, B. Ratiu, W. Zhang, O. Abouzaid, ... and Q. Li, "Lateral Tunnel Epitaxy of GaAs in Lithographically Defined Cavities on 220 nm Silicon-on-Insulator", Cryst. Growth Des. 2023, 23, 7821−7828.

26. Y. Han, Z. Yan, Y. Xue, and K. M. Lau, "Micrometer-scale InP selectively grown on SOI for fully integrated Si-photonics", Appl. Phys. Lett. 117, 052102 (2020).

27. D. Fu, Z. Ren, Y. Jin, Y. Han, and S. Yu, "Buried InGaAs/InP quantum wells selectively grown on SOI for lateral membrane laser diodes", Appl. Phys. Lett. 124, 081102 (2024).

28. H. Homma, H. Sugiyama, T. Hiraki, T. Sato, and S. Matsuo, "Microstructural characterization of InP films on SOI (001) substrates grown by selective lateral metal-Organic vapor-Phase epitaxy", Journal of Crystal Growth 648 (2024) 127903.

29. D. Fu, Y. Chen, Z. Ren, Y. Zhao, ... and S. Yu, "Engineering downward-propagating threading dislocations for InP lasers laterally grown on 220 nm SOI", Opt. Express 33, 13280-13286 (2025).

30. Z. Yan, W. Zang, M. Ebert, B. Ratiu, ... and Q. Li, "Integrating InP membranes on silicon-on-insulator via tunnel epitaxy for silicon photonics", Photon. Res. 14, 123-129 (2026)

31. Z. Yan, Y. Han and K. Lau, "Multi-heterojunction InAs/GaSb nano-ridges directly grown on (001) Si", Nanotechnology 31 (2020) 345707 (7pp).

32. Z. Yan, Y. Han, and K. M. Lau, "InAs nano-ridges and thin films grown on (001) silicon substrates", J. Appl. Phys. 128, 035302 (2020).

33. Z. Lei, D. Fu, Y. Han, and S. Yu, "Strain engineering of vertical (110) InGaAs/InP quantum wells laterally grown on (001) SOI", Appl. Phys. Lett. 126, 182104 (2025).

34. Z Wu, Z. Lei, Z. Ren, C. Zeng, ... and S. Yu, "Continuous-wave III–V micro-ring lasers with position-controlled vertical QWs laterally integrated on SOI", Photon. Res. 13, 3492-3498 (2025)

35. T. Hammerschmidt, P. Kratzer, and M. Scheffler, "Elastic response of cubic crystals to biaxial strain: Analytic results and comparison to density functional theory for InAs", PHYSICAL REVIEW B 75, 235328 2007

36. K. E. MacArthur, A. B. Yankovich, A. Béché, M. Luysberg, ... and L. J. Allen, "Optimizing Experimental Conditions for Accurate Quantitative Energy-Dispersive X-ray Analysis of Interfaces at the Atomic Scale", Microscopy and Microanalysis (2021), 27, 528–542

37. F. Bugge, M. Zorn, U. Zeimer, T. Sharma, ... and M. Weyers, "Highly strained very high-power laser diodes with InGaAs QWs", Journal of Crystal Growth 248 (2003) 354–358